

This document contains a post-print version of the paper

Model-based control concepts for vibratory MEMS gyroscopes

authored by M. Egretzberger, F. Mair, A. Kugi

and published in *Mechatronics*.

The content of this post-print version is identical to the published paper but without the publisher's final layout or copy editing. Please, scroll down for the article.

Cite this article as:

M. Egretzberger, F. Mair, A. Kugi, "Model-based control concepts for vibratory mems gyroscopes", *Mechatronics*, 22, 3, 241–250, 2012. DOI: [10.1016/j.mechatronics.2011.06.003](https://doi.org/10.1016/j.mechatronics.2011.06.003)

BibTex entry:

```
@article{acinpaper,  
  author = {Egretzberger, M. and Mair, F. and Kugi, A.},  
  title = {Model-based control concepts for vibratory MEMS gyroscopes},  
  journal = {Mechatronics},  
  year = {2012},  
  volume = {22},  
  number = {3},  
  pages = {241--250},  
  doi = {10.1016/j.mechatronics.2011.06.003},  
  url = {http://www.sciencedirect.com/science/article/pii/S0957415811001048}  
}
```

Link to original paper:

<http://dx.doi.org/10.1016/j.mechatronics.2011.06.003>
<http://www.sciencedirect.com/science/article/pii/S0957415811001048>

Read more ACIN papers or get this document:

<http://www.acin.tuwien.ac.at/literature>

Contact:

Automation and Control Institute (ACIN)
Vienna University of Technology
Gusshausstrasse 27-29/E376
1040 Vienna, Austria

Internet: www.acin.tuwien.ac.at
E-mail: office@acin.tuwien.ac.at
Phone: +43 1 58801 37601
Fax: +43 1 58801 37699

Copyright notice:

This is the authors' version of a work that was accepted for publication in *Mechatronics*. Changes resulting from the publishing process, such as peer review, editing, corrections, structural formatting, and other quality control mechanisms may not be reflected in this document. Changes may have been made to this work since it was submitted for publication. A definitive version was subsequently published in M. Egretzberger, F. Mair, A. Kugi, "Model-based control concepts for vibratory mems gyroscopes", *Mechatronics*, 22, 3, 241–250, 2012. DOI: [10.1016/j.mechatronics.2011.06.003](https://doi.org/10.1016/j.mechatronics.2011.06.003)

Model-based Control Concepts for Vibratory MEMS Gyroscopes

Markus Egretzberger, Florian Mair, Andreas Kugi

*Vienna University of Technology, Automation and Control Institute,
Gusshausstraße 27-29, 1040 Wien, Austria*

Abstract

In this contribution, a systematic method for the design of open- and closed-loop controllers for vibratory MEMS gyroscopes based on so-called envelope models will be presented. The methodology will be exemplarily carried out for a gyroscope with electrostatic actuation and read-out elements. The specifically designed capacitive actuators of the gyroscope are capable of compensating the system's inherent mechanical unbalance (quadrature compensation) as well as the system's response to an external angular rate (force feedback). The utilized envelope model solely captures the relevant system dynamics of the gyroscope while at the same time describing the actuation and read-out mechanisms simplified to a suitable level of detail thus providing the basis for an efficient and systematic control design.

In order to demonstrate the proposed methodology, an optimized start-up strategy for the control of the primary oscillation is designed. Furthermore, the approach is utilized for the deviation of a basic quadrature controller for the secondary oscillation. In order to account for the typically weakly damped open-loop dynamics of the gyroscope and the transient coupling between the quadrature and the angular rate signal a more sophisticated combined concept of closed-loop quadrature and force feedback control is introduced. Both simulation and measurement results obtained for a prototype gyroscope validate the mathematical models and prove the feasibility of the proposed concepts.

Keywords: MEMS gyroscopes, envelope model, capacitive sensors and actuators, quadrature error, force feedback.

Preprint submitted to Mechatronics

May 17, 2011

1. Introduction

Vibratory micro electromechanical gyroscopes are typically driven by a primary oscillator. This primary oscillation is usually excited close to the resonance frequency in order to achieve maximum amplitudes. Similar to many electronic circuits, in particular in information technology, the wanted signals are modulated in a high-frequency carrier signal. Hence, the rate of change of the wanted signals is several orders of magnitude slower than the carrier frequency itself. In the case of vibratory micro electromechanical gyroscopes an external angular rate causes a secondary oscillation with an amplitude proportional to the angular rate component about the sensitive axis by exploiting the Coriolis effect. The output signal of the sensor (i.e., the angular rate) is obtained by an appropriate demodulation of the secondary oscillation signal. In order to provide a linear sensor behavior and maximum sensitivity, the frequency and amplitude of the primary oscillation have to be controlled. Furthermore, micro electromechanical gyroscopes are subject to large quadrature errors due to limitations in the fabrication process. These quadrature errors are due to a mechanical unbalance, which causes a coupling between the primary and secondary oscillation without the presence of an external angular rate. This quadrature signal can be separated from the angular rate signal after the demodulation of the secondary oscillation. In order to avoid a drift of the output signal, e.g., over temperature, due to demodulation errors the mechanical unbalance has to be actively compensated. Therefore, an additional actuation of the secondary oscillator has to be provided such that a controller can be implemented to suppress the unwanted quadrature signal. Furthermore, in order to increase the bandwidth of the MEMS gyroscope so-called force feedback controllers are utilized to additionally compensate the response to the external angular rate.

In this context, many articles dealing with the control of vibratory gyroscopes can be found in the literature, see, e.g., [1, 2, 3, 4, 5]. All of the mentioned control loops have in common that the relevant closed-loop dynamics lie within the frequency range of the envelope of the signal rather than in the frequency range of the carrier signal itself. In particular from a system analysis and control design point of view, this motivates to derive a more comprehensive mathematical model which solely captures the essential "slow" dynamics (envelope) of the system as proposed in [6].

In this contribution, the simplified envelope model introduced for vibratory gyroscopes in [6] will be used as the basis for the design of suitable

control concepts. The presented methodology will be exemplarily carried out for a capacitive MEMS gyroscope. Thereby, the paper is organized as follows: In Sec. 2, the working principle of vibratory gyroscopes is discussed in terms of the specific capacitive device under consideration. Furthermore, a suitable mathematical model in terms of a simplified envelope model is presented in order to describe the essential dynamics of the primary and secondary oscillation. Based on this simplified envelope model, Sec. 3 is devoted to the derivation of suitable open- and closed-loop controllers for both the primary and the secondary oscillation including an optimized start-up strategy as well as the unbalance compensation and the force feedback of the angular rate response. Measurement results are presented in Sec. 4 and the paper concludes with a short summary.

2. A capacitive gyroscope

The micro electromechanical device being considered in this paper is a gyroscope consisting of a plane symmetric silicon structure operating with an in-plane primary mode, excited by capacitive comb actuators, and an out-of-plane secondary mode with capacitive parallel plate sensors. Most capacitive gyroscopes found in the literature are driven by electrostatic comb actuators bringing about the advantage of a high actuation stroke and little required space. They are found in linear oscillating as well as in rotating designs, see, e.g., [7, 8, 9, 10]. For the same reason, the read-out of the secondary oscillation is preferably also realized by means of comb sensors. Obviously, comb sensors require the secondary mode to be an in-plane oscillation as it is the case for the designs presented in [8, 9]. If the secondary mode is an out-of-plane oscillation, parallel plate capacitors are more suitable since the movable electrodes are designed to be part of the oscillating structure and the corresponding fixed electrodes are directly mounted on the housing of the device, see, e.g., [11].

Within the scope of this work, let us restrict ourselves to one specific design of a capacitive gyroscope as presented in Fig. 1 which is an enhanced version of the gyroscope presented in [11]. This design is capable of both compensating the mechanical unbalance and realizing a force feedback. In this section, the working principle of the capacitive gyroscope is explained first and afterwards the appropriate mathematical model for the controller design will be formulated.

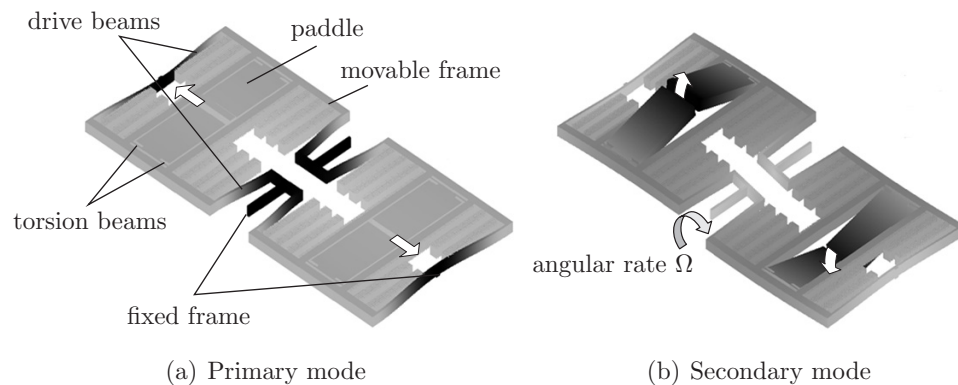


Figure 1: Schematics of the capacitive gyroscope.

2.1. Principle of operation

The capacitive gyroscope as depicted in Fig. 1 is an etched, plane silicon structure possessing two axes of symmetry. It consists of a rectangular fixed frame, which is rigidly mounted on the housing of the device, and two movable frames, one on the left and one on the right half of the sensor, which are flexibly connected to the fixed frame via elastic beams, the so-called drive beams. Moreover, two paddles are flexibly connected to each movable frame via torsion beams.

The comb actuators and comb sensors comprise electrodes on the fixed frame and on the corresponding movable frames. The comb actuators allow for a harmonic excitation of the movable frames and the paddles in an anti-symmetric in-plane oscillation (primary mode). If an external angular rate Ω is applied to the system, the Coriolis force is coupling to the velocity of the movable frames and paddles causing an out-of-plane motion of these elements (secondary mode). The comb sensors provide the feedback signal for the amplitude control of the primary mode, while the secondary mode is measured by means of four parallel plate capacitors with fixed electrodes placed on the housing above each paddle. The mechanical unbalance, which causes an additional (unwanted) coupling between the primary and the secondary mode, originates from a distortion of the rectangular shaped cross sections of the beam elements, in particular at the drive beams. In the mathematical model provided below this effect will be accounted for by means of beam elements with rhomboid cross sections characterized by the so-called side wall angle ξ , see [12]. Furthermore, there are capacitive paral-

lel plate actuators provided for the excitation of the secondary mode, each consisting of several fixed electrodes placed above the movable frame and the paddles. These additional actuators are intended for the active compensation of the mechanical unbalance as well as for the force feedback of the angular rate. All electrostatic actuators are assumed to be voltage controlled with a desired input voltage, see, e.g., [13]. The electrostatic sensors are realized by means of so-called charge amplifier circuits to convert the capacitance change into a proportional output voltage. These circuits are complemented by appropriate differential amplifiers in order to obtain suitable output signals for the primary and secondary mode.

2.2. Dynamical model

As described in Sec. 2.1 the micro electromechanical device is composed of several components, i.e., the movable mechanical structure consisting of rigid elements (movable frame, paddles), elastic elements (beam structures) and the electrostatic actuators (comb and parallel plate capacitors). In a more general form, the capacitive gyroscope can be considered as a multi-body system made up of rigid and elastic bodies with external forces applied by the capacitive actuators. The equations of motion can be systematically derived by means of Lagrange's formalism, e.g., by utilizing the approach presented in [14]. The thus resulting model is in general a complex system of non-linear ordinary differential equations as presented in [6]. However, if only the principal modes of operation are considered the resulting dynamical system can be written in the simplified form, see [6],

$$\begin{bmatrix} m_1 & 0 \\ 0 & m_2 \end{bmatrix} \begin{bmatrix} \ddot{q}_1 \\ \ddot{q}_2 \end{bmatrix} + \begin{bmatrix} d_1 & -c_{12}\Omega \\ c_{12}\Omega & d_2 \end{bmatrix} \begin{bmatrix} \dot{q}_1 \\ \dot{q}_2 \end{bmatrix} + \begin{bmatrix} k_1 & \xi k_{12} \\ \xi k_{12} & k_2 \end{bmatrix} \begin{bmatrix} q_1 \\ q_2 \end{bmatrix} = \begin{bmatrix} f_1 \\ f_2 \end{bmatrix} \quad (1)$$

with the primary mode q_1 and the secondary mode q_2 as well as the inertia, damping and stiffness coefficients m_j , d_j and k_j with $j = 1, 2$ and the coupling coefficients due to the Coriolis force and the mechanical unbalance c_{12} and k_{12} , respectively. The left-hand side of (1) is the typical representation of a simple autonomous mechanical model for vibratory MEMS gyroscopes, see, e.g., [15], while the electromechanical coupling forces f_1 and f_2 on the right-hand side strongly depend on the specific design of the electrostatic actuators as will be outlined in more detail below.

For the capacitive gyroscope under consideration, the comb capacitors actuating the primary mode are specifically designed to generate an input force

f_1 independent of the mechanical deflection (i.e. the primary and secondary modes q_1 and q_2) of the form $f_1 = b_1 u_P^2$, see, e.g. [11], with the constant parameter b_1 and the primary input voltage u_P such that the equation of motion for the primary mode can be written as

$$m_1 \ddot{q}_1 + d_1 \dot{q}_1 + k_1 q_1 - \Omega c_{12} \dot{q}_2 + \xi k_{12} q_2 = b_1 u_P^2. \quad (2)$$

The amplitudes of the primary mode q_1 excited by the input voltage u_P are typically several orders of magnitude larger than the amplitudes of the secondary mode excited by the weak coupling to the primary mode due to the Coriolis force and the mechanical unbalance. Hence, for the purpose of system analysis and control design it is reasonable to assume that the coupling terms from the secondary to the primary mode $\Omega c_{12} \dot{q}_2$ and $\xi k_{12} q_2$ in (2) are considerably small and thus can be neglected.

In contrast to the actuation of the primary mode, the parallel plate actuators for the additional excitation of the secondary mode (intended for unbalance compensation and force feedback, see Sec. 2.1) are deliberately designed to generate an input force f_2 which specifically depends on the mechanical deflections q_1 and q_2 yielding a nonlinear relation of the form $f_2(q_1, q_2, u_{S,1}, \dots, u_{S,m})$, with the secondary input voltages $u_{S,i}$, $i = 1, \dots, m$. The mathematical structure of the nonlinear term f_2 strongly relies on the actual placement and orientation of the electrostatic actuators as will be seen below.

Considering these actuators as parallel plate capacitors with rectangular electrodes, as shown in Fig. 2 for the i -th actuator, it is assumed that the movable electrode possesses two translational degrees-of-freedom, i.e. the displacements x_i and z_i of the center point aligned with the principal directions of the primary and secondary motion, respectively. Thus, if no other modes are excited the degrees-of-freedom can be written as $x_i = \pm r_i q_1$ and $z_i = \mp s_i q_2$ with the positive constants r_i and s_i . The capacitance C_i and the potential energy W_i of the i -th actuator is then given by

$$C_i = \varepsilon_0 \frac{A_i + x_i t_i}{g_i - z_i} = \varepsilon_0 \frac{A_i \pm r_i t_i q_1}{g_i \pm s_i q_2}, \quad W_i = \frac{1}{2} C_i u_{S,i}^2 \quad (3)$$

with the dielectric coefficient ε_0 , the gap g_i , the width t_i , the overlap area $A_i = t_i l_i$ and the overlap length l_i in the undeformed configuration, see Fig. 2. The nonlinear input term f_2 in (1) is calculated as

$$f_{2,i} = \frac{\partial W_i}{\partial q_2} = \mp \frac{1}{2} \frac{\varepsilon_0 s_i (A_i \pm r_i t_i q_1)}{(g_i \pm s_i q_2)^2} u_{S,i}^2, \quad f_2 = \sum_{i=1}^m f_{2,i}. \quad (4)$$

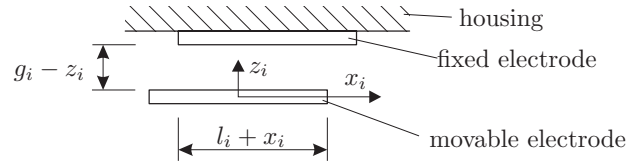


Figure 2: Parallel plate capacitor.

From (3) and (4) it can be seen that, depending on the geometric design of the actuators, the secondary mode can be excited by a nonlinear term f_2 possessing four different algebraic sign permutations.

The specific gyroscope under consideration, see [11], however, is designed such that $m = 4$ capacitive parallel plate actuators generate an input term of the form

$$f_2 = \frac{\varepsilon_0}{2} \left(\frac{s_1 (A_1 + r_1 t_1 q_1)}{(g_1 - s_1 q_2)^2} u_{S,1}^2 - \frac{s_2 (A_2 + r_2 t_2 q_1)}{(g_1 + s_2 q_2)^2} u_{S,2}^2 + \frac{s_3 (A_3 - r_3 t_3 q_1)}{(g_1 - s_3 q_2)^2} u_{S,3}^2 - \frac{s_4 (A_4 - r_4 t_4 q_1)}{(g_1 + s_4 q_2)^2} u_{S,4}^2 \right). \quad (5)$$

Substituting the input transformation

$$\begin{aligned} u_{S,1} &= \sqrt{\tilde{u}_T - \tilde{u}_C + \tilde{u}_S}, & u_{S,2} &= \sqrt{\tilde{u}_T + \tilde{u}_C - \tilde{u}_S}, \\ u_{S,3} &= \sqrt{\tilde{u}_T + \tilde{u}_C + \tilde{u}_S}, & u_{S,4} &= \sqrt{\tilde{u}_T - \tilde{u}_C - \tilde{u}_S} \end{aligned} \quad (6)$$

into (5) and linearizing with respect to q_1 and q_2 about the point $q_1 = q_2 = 0$ yields an approximation valid for small displacements. If all of the four actuators possess the same gaps $g = g_i$ and the geometrical conditions $sA = s_i A_i$, $r s t = r_i s_i t_i$ and $s^2 A = s_i^2 A_i$ for $i = 1, \dots, 4$ hold (symmetry), the linear approximation is given by

$$f_2 \simeq \underbrace{\frac{2\varepsilon_0 s A}{g^2}}_{b_2} \tilde{u}_S - \underbrace{\frac{2\varepsilon_0 r s t}{g^2}}_{k_{12,C}} q_1 \tilde{u}_C + \underbrace{\frac{4\varepsilon_0 s^2 A}{g^3}}_{k_{2,T}} q_2 \tilde{u}_T. \quad (7)$$

By making use of the approximation (7) the equation of motion of the secondary mode according to (1) can be rewritten as

$$m_2 \ddot{q}_2 + d_2 \dot{q}_2 + (k_2 - k_{2,T} \tilde{u}_T) q_2 + \Omega c_{12} \dot{q}_1 + (k_{12} + k_{12,C} \tilde{u}_C) q_1 = b_2 \tilde{u}_S, \quad (8)$$

with the constant coefficients b_2 , $k_{12,C}$ and $k_{2,T}$. It can be seen that the new control inputs \tilde{u}_S , \tilde{u}_C and \tilde{u}_T are decoupled with \tilde{u}_S allowing for a harmonic excitation of the secondary mode, \tilde{u}_C serves for the compensation of the unbalance and \tilde{u}_T allows for the tuning of the stiffness and thus the resonance frequency of the secondary mode.

2.3. Envelope model

In the following, it is assumed that the primary mode is harmonically excited by applying an input voltage of the form $u_P = U_{P,0} + U_{P,C} \cos(\omega t)$ to the capacitive comb actuators with $U_{P,0} \geq U_{P,C}$. The excitation frequency ω is chosen to be close to the eigenfrequency of the primary mode ω_1 in order to achieve maximum amplitudes. As is shown in detail in [6] it is reasonable to introduce a so-called envelope model for the harmonically excited and weakly damped resonance structure under consideration. Especially for the purpose of system analysis and control design this modeling technique has the advantage of reducing the overall dynamical system to a system with a manageable number of degrees-of-freedom solely describing the essential (slow) dynamics of the corresponding envelopes. Henceforth, the primary and secondary mode are approximated in the form $q_j = Q_{j,S} \sin(\omega t) + Q_{j,C} \cos(\omega t)$, $j = 1, 2$ with the Fourier coefficients $Q_{j,S}$ and $Q_{j,C}$, while the dc-components and the higher harmonics are assumed to be negligible.

The envelope models of the primary and secondary mode corresponding to the dynamical systems (2) and (8) describing the dynamics of the Fourier coefficients $Q_{j,S}$ and $Q_{j,C}$ can be derived according to [6] and are shortly recapitulated in the following two subsections.

2.3.1. Primary mode

Neglecting the weak coupling terms due to the angular rate Ω and the side wall angle ξ in (2) the envelope model of the primary mode describing the dynamics of $Q_{1,S}$ and $Q_{1,C}$ is given by, see [6, 16],

$$\frac{d}{dt} \begin{bmatrix} Q_{1,S} \\ Q_{1,C} \end{bmatrix} = \begin{bmatrix} -\alpha_1 & \omega - \omega_1 \\ -\omega + \omega_1 & -\alpha_1 \end{bmatrix} \begin{bmatrix} Q_{1,S} \\ Q_{1,C} \end{bmatrix} - \begin{bmatrix} \beta_1 \\ 0 \end{bmatrix} \tilde{U}_{P,C} \quad (9)$$

and the output $Y_{P,\beta} = c_1 Q_{1,\beta}$, $\beta \in \{S, C\}$ corresponds to the Fourier coefficients of the primary output voltage $y_P = c_1 q_1$ with the constant parameter c_1 . The component $\tilde{U}_{P,C} = 2 U_{P,0} U_{P,C}$ stems from the quadratic input non-linearity of the capacitive actuators. Furthermore, the damping coefficient

α_1 , the eigenfrequency ω_1 and the input coefficient β_1 of the primary mode are given by the relations, see [6, 16],

$$\alpha_1 = \frac{1}{2} \frac{d_1}{m_1}, \quad \omega_1 = \frac{1}{2} \frac{1}{m_1} \sqrt{4k_1 m_1 - d_1^2}, \quad \beta_1 = \frac{1}{2} \frac{b_1}{m_1 \omega_1}.$$

For the control design, it is beneficial to introduce an output transformation to polar coordinates in the form

$$Y_{P,A} = \sqrt{Y_{P,S}^2 + Y_{P,C}^2}, \quad Y_{P,\varphi} = \arctan\left(\frac{Y_{P,S}}{Y_{P,C}}\right) \quad (10)$$

with the amplitude $Y_{P,A}$ and the phase $Y_{P,\varphi}$ of the primary output voltage. In steady state, the amplitude and phase of the primary output voltage read as

$$Y_{P,A} = \frac{\beta_1 c_1 \tilde{U}_{P,C}}{\sqrt{\alpha_1^2 + (\omega - \omega_1)^2}}, \quad Y_{P,\varphi} = \arctan\left(\frac{\alpha_1}{\omega_1 - \omega}\right).$$

Clearly, the maximum amplitude $Y_{P,A}$ in steady state is obtained for the angular velocity $\omega = \omega_1$ where at the same time the phase is $Y_{P,\varphi} = -\pi/2$. Hence, the first two tasks concerning the control of the primary mode can be formulated as follows. The output phase $Y_{P,\varphi}$ must be controlled to $-\pi/2$ and the output amplitude $Y_{P,A}$ to a predefined constant value $Y_{P,des}$.

2.3.2. Secondary mode

Now, let us assume that the primary mode is ideally controlled with $Y_{P,A} = Y_{P,des}$ and $Y_{P,\varphi} = -\pi/2$ yielding the steady state $Q_{1,S} = Y_{P,des}/c_1$ and $Q_{1,C} = 0$. If the trimming and compensation inputs introduced in (6) are slowly varying signals $\tilde{u}_T = \tilde{U}_T$ and $\tilde{u}_C = \tilde{U}_C$ and the excitation input is a harmonic signal of the form $\tilde{u}_S = \tilde{U}_{S,C} \cos(\omega_1 t)$ the envelope model of the secondary mode model (8) can be written as, see [6, 16],

$$\frac{d}{dt} \begin{bmatrix} Q_{2,S} \\ Q_{2,C} \end{bmatrix} = \begin{bmatrix} -\alpha_2 & \omega_1 - \omega_2 \\ -\omega_1 + \omega_2 & -\alpha_2 \end{bmatrix} \begin{bmatrix} Q_{2,S} \\ Q_{2,C} \end{bmatrix} + \beta_{12} \begin{bmatrix} \Omega - \Gamma_F \tilde{U}_{S,C} \\ \Gamma_M + \Gamma_C \tilde{U}_C \end{bmatrix}, \quad (11)$$

with the output $Y_{S,\beta} = c_2 Q_{2,\beta}$, $\beta \in \{S, C\}$ denoting the Fourier coefficients of the secondary output voltage $y_S = c_2 q_2$, the damping coefficient α_2 and the eigenfrequency ω_2 of the secondary mode

$$\alpha_2 = \frac{1}{2} \frac{d_2}{m_2}, \quad \omega_2 = \frac{1}{2} \frac{1}{m_2} \sqrt{4(k_2 - k_{2,T} \tilde{U}_T) m_2 - d_2^2},$$

respectively and the input coefficients

$$\beta_{12} = \frac{1}{2} \frac{\omega_1}{\omega_2} \frac{c_{12} Y_{P,des}}{c_1 m_2}, \quad \Gamma_F = \frac{b_2 c_1}{\omega_1 c_{12} Y_{P,des}},$$

$$\Gamma_M = \frac{k_{12} \xi}{\omega_1 c_{12}}, \quad \Gamma_C = \frac{k_{12,C}}{\omega_1 c_{12}}.$$

In order to separate the response due to the external angular rate from the response due to the mechanical unbalance in the output $\mathbf{Y} = [Y_{S,S}, Y_{S,C}]^T$, a transformation $\mathbf{Z} = \mathbf{T} \mathbf{Y}$ of the form

$$\mathbf{T} = \begin{bmatrix} \sin(\phi) & \cos(\phi) \\ \cos(\phi) & -\sin(\phi) \end{bmatrix}, \quad \phi = \arctan\left(\frac{\alpha_2}{\omega_2 - \omega_1}\right), \quad (12)$$

with the new output $\mathbf{Z} = [Z_{S,R}, Z_{S,Q}]^T$, is performed. Then, the steady state of the system (11) with the output transformation (12) yields the Fourier coefficients of the transformed output signals

$$Z_{S,R} = S (\Omega - \Gamma_F \tilde{U}_{S,C}), \quad Z_{S,Q} = -S (\Gamma_M + \Gamma_C \tilde{U}_C) \quad (13)$$

with the sensitivity

$$S = \frac{\beta_{12} c_2}{\sqrt{\alpha_2^2 + (\omega_1 - \omega_2)^2}}.$$

In the output \mathbf{Z} , the system (11) is stationarily decoupled and the components $Z_{S,R}$ and $Z_{S,Q}$ are denoted as the angular rate and the quadrature signal, respectively. It can be seen from (13) that the mechanical unbalance is compensated for $\Gamma_C \tilde{U}_C = -\Gamma_M$, achieved by controlling the quadrature signal $Z_{S,Q}$ to zero. The angular rate signal $Z_{S,R}$ either serves as the measurement output of the MEMS gyroscope or is compensated in the form $\Gamma_F \tilde{U}_{S,C} = \Omega$ in the case of force feedback control.

3. Control design

Within the scope of this paper the systematic design of open- and closed-loop controllers is exemplarily carried out for the control tasks formulated in the previous section, i.e., the amplitude and phase control of the primary mode and the quadrature and force feedback control of the secondary mode. The theoretical concepts are verified by means of numerical simulations utilizing a simulation model with a high level of detail, see [6], and by means of measurement results on a prototype gyroscope.

3.1. Control of the primary oscillation

A main objective of the primary control concept is the optimized start-up of the primary oscillation in the presence of parameter uncertainties. In particular the reference frequency provided by a quartz oscillator as well as the eigenfrequencies of the gyroscopes are subject to fabrication tolerances and to significant drifts due to the dependence of the material parameters on the temperature. A suitable solution for the start-up of the primary oscillation is a sinusoidal sweep from a start frequency ω_0 chosen to cover the worst case scenario for the smallest possible primary eigenfrequency and the maximum specified tolerance of the quartz oscillator. Then, the excitation is carried out in the form

$$U_{P,0} = U_{P,C} = \frac{1}{2} U_{P,max} , \quad \omega = \omega_0 + \zeta_S t , \quad t > 0 \quad (14)$$

with the frequency slope ζ_S and the maximum possible primary excitation voltage $U_{P,max}$. The simulated transient response with $\omega_0 = 0.98\omega_1$ and $\zeta_S = 2 \text{ kHz/s}$ in terms of the amplitude $Y_{P,A}$ and the phase $Y_{P,\varphi}$ is illustrated in Fig. 3(a) and respectively Fig. 3(b). There, the amplitude is normalized with respect to the desired amplitude $Y_{P,des}$ in steady state in the form $\tilde{Y}_{P,A} = Y_{P,A}/Y_{P,des}$. The circles in Fig. 3 indicate the amplitude and phase of the primary output voltage at the time $t = t_S$ when the phase is crossing the value of $-\pi/2$ for the first time (apart from a short settling phase $0 \leq t \leq t_0$ that is neglected). The corresponding angular frequency at this time is $\omega_S = \omega(t_S)$. If the sinusoidal sweep is performed for gyroscopes possessing different quality factors $Q_1 = \omega_1/(2\alpha_1)$, it turns out that the difference between ω_S and the primary eigenfrequency ω_1 remains nearly constant, see Fig. 3(c). Since the identified frequency difference $\omega_S - \omega_1$ is nearly independent of the quality factor Q_1 for each slope ζ_S , the primary eigenfrequency can be estimated at $t = t_S$ in the form

$$\omega_1 \simeq \bar{\omega}_1 = \omega_S - \Delta\omega_S, \quad (15)$$

with $\Delta\omega_S$ being the nominal frequency difference for each slope ζ_S . The choice of the maximum possible slope is limited by the minimum necessary signal amplitude in order to achieve a proper signal-to-noise ratio.

The control design is now based on the system (9) starting from the initial condition at $t = t_S$ with $Y_{P,A} > 0$ and $Y_{P,\varphi} = -\pi/2$. If the angular frequency is chosen as $\omega = \omega_1$ for $t > t_S$ the component $Q_{1,C}$ remains in the steady state, i.e., the desired trajectory is $Q_{1,C}^* = 0$ with the output $Y_{P,\varphi}^* = -\pi/2$.

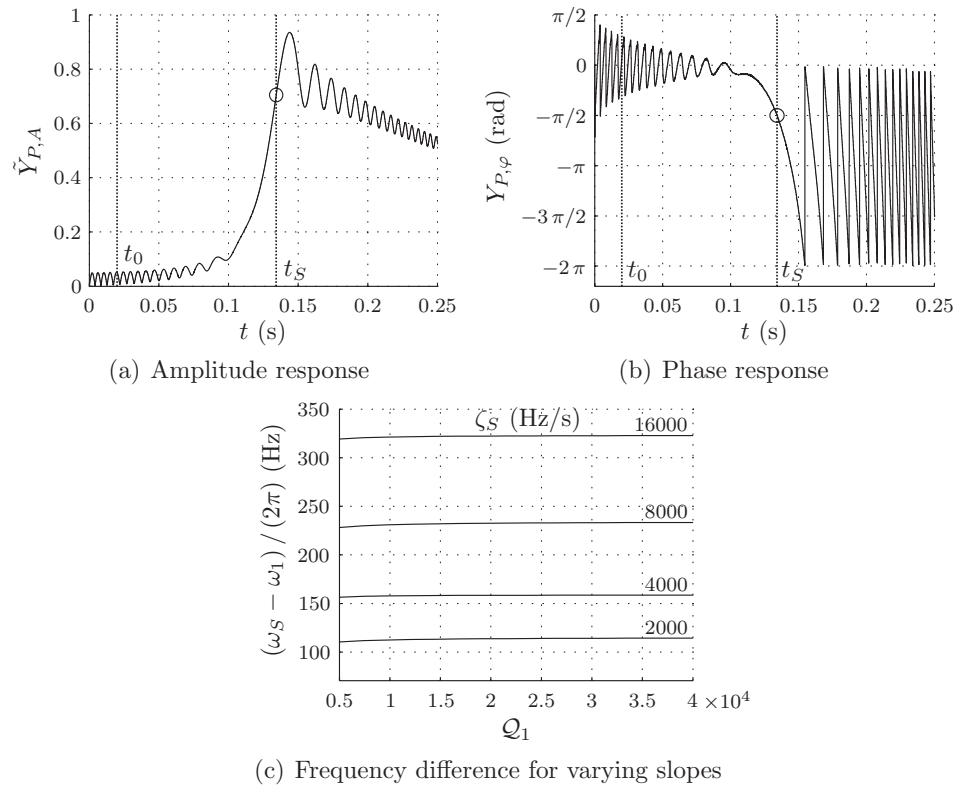


Figure 3: Transient response of the primary output voltage due to a sinusoidal sweep in terms of (a) the amplitude $\tilde{Y}_{P,A}$ (b) the phase $Y_{P,\varphi}$, and (c) the frequency difference $\omega_S - \omega_1$ for varying slopes ζ_S over the quality factor Q_1 .

Then, the (time optimal) control for the residual first order system, see (9),

$$\frac{d}{dt} Q_{1,S}^* = -\alpha_1 Q_{1,S}^* - \beta_1 \tilde{U}_{P,C}^*$$

is given by the maximum possible constant input $\tilde{U}_{P,C}^*$ until the trajectory $Y_{P,A}^* = c_1 Q_{1,S}^*$ has reached the desired amplitude $Y_{P,des}$ at the time $t = t_A$. For $t \geq t_A$, we aim at staying in the steady state $Y_{P,A}^* = Y_{P,des}$. This is achieved for the feedforward control input

$$\omega^* = \omega_1, \quad t_S \leq t \quad \text{and} \quad \tilde{U}_{P,C}^* = \begin{cases} \frac{1}{2} U_{P,max}^2 & t_S \leq t < t_A \\ -\frac{\alpha_1}{\beta_1 c_1} Y_{P,des} & t \geq t_A \end{cases} \quad (16)$$

In reality, however, the real model parameters $\hat{\alpha}_1$, $\hat{\omega}_1$, $\hat{\beta}_1$ and \hat{c}_1 differ from the nominal values α_1 , ω_1 , β_1 and c_1 . Thus, it is reasonable to substitute the estimation $\bar{\omega}_1$ for the primary eigenfrequency ω_1 , cf. (15), in the feedforward control (16), i.e., $\omega^* = \omega_S - \Delta\omega_S$, while the input $\tilde{U}_{P,C}^*$ can only be calculated for the nominal parameter values α_1 , β_1 and c_1 . Therefore, a drift of the phase $Y_{P,\varphi}$ and the amplitude $Y_{P,A}$ is inevitable, which necessitates the design of a suitable closed-loop control.

After the sinusoidal sweep for the time $0 \leq t < t_S$, the second stage of the primary control is the phase control, where the excitation frequency is composed of the feedforward and feedback control inputs ω^* and $\Delta\omega$ in the form

$$\omega = \omega^* + \Delta\omega \quad \text{for} \quad t \geq t_S \quad (17)$$

During this control stage the maximum possible primary input voltage $\tilde{U}_{P,C}^* = U_{P,max}^2/2$ is applied until the desired amplitude $Y_{P,des}$ is reached at $t = t_A$. Then, in the third stage, i.e. for $t \geq t_A$, a combined phase and amplitude control is performed. For the feedback control of the amplitude, a new input $\Delta\tilde{U}_{P,C}$ is introduced yielding the coefficients of the primary excitation voltage in the form

$$U_{P,C} = \begin{cases} \frac{1}{2} U_{P,max} \\ U_{P,ctrl} \end{cases} \quad U_{P,0} = \begin{cases} \frac{1}{2} U_{P,max} & t_S \leq t < t_A \\ \frac{1}{2} \frac{\tilde{U}_{P,C}^* + \Delta\tilde{U}_{P,C}}{U_{P,ctrl}} & t \geq t_A \end{cases} \quad (18)$$

with a suitable constant parameter $U_{P,ctrl}$.

For the design of the feedback controller, the system (9) with output (10) is linearized around the desired operating point $Q_{1,S}^* = Y_{P,des}/c_1$, $Q_{1,C}^* = 0$, $\omega^* = \omega_1$ and $\tilde{U}_{P,C}^* = -\alpha_1 Y_{P,des}/(\beta_1 c_1)$ yielding a linear time-invariant system of the form

$$\frac{d}{dt} \begin{bmatrix} \Delta Q_{1,S} \\ \Delta Q_{1,C} \end{bmatrix} = - \begin{bmatrix} \alpha_1 & 0 \\ 0 & \alpha_1 \end{bmatrix} \begin{bmatrix} \Delta Q_{1,S} \\ \Delta Q_{1,C} \end{bmatrix} - \begin{bmatrix} 0 & \beta_1 \\ Q_{1,S}^* & 0 \end{bmatrix} \begin{bmatrix} \Delta \omega \\ \Delta \tilde{U}_{P,C} \end{bmatrix} \quad (19a)$$

with the output

$$\begin{bmatrix} \Delta Y_{P,A} \\ \Delta Y_{P,\varphi} \end{bmatrix} = \begin{bmatrix} c_1 & 0 \\ 0 & -1/Q_{1,S}^* \end{bmatrix} \begin{bmatrix} \Delta Q_{1,S} \\ \Delta Q_{1,C} \end{bmatrix} \quad (19b)$$

and the deviations $\Delta Q_{1,S}$, $\Delta Q_{1,C}$, $\Delta Y_{P,A}$ and $\Delta Y_{P,\varphi}$ from the operating point. It can be seen that the linearized system (19) is decoupled from the control input $\Delta \omega$ and $\Delta \tilde{U}_{P,C}$ to the output $\Delta Y_{P,\varphi}$ and $\Delta Y_{P,A}$ with the corresponding transfer functions

$$G_{P,\varphi}(s) = \frac{1}{s + \alpha_1}, \quad G_{P,A}(s) = -\frac{\beta_1 c_1}{s + \alpha_1}, \quad (20)$$

and the Laplace variable s . Based on (20) two PI-controllers are designed by means of the loop-shaping method in such a way that the rise times of the closed-loop step responses become considerably small without entailing an overshooting. This linearized approach is reasonable as long as the deviations are sufficiently small. It has proven robust against parameter variations and different frequency slopes of the sinusoidal sweep, see also the measurement results in Sec. 4.

Summarizing, the start-up control strategy for the primary oscillation can be separated into three phases, namely the sinusoidal sweep (stage I, $0 \leq t \leq t_S$), the open-loop amplitude and closed-loop phase control (stage II, $t_S < t \leq t_A$) and the closed-loop amplitude and phase control (stage III, $t > t_A$). The corresponding simulation results in terms of the output signals $\tilde{Y}_{P,A}$ and $Y_{P,\varphi}$ and the corresponding control inputs $U_{P,0}$, $U_{P,C}$ and ω are depicted in Fig. 4. The frequency slope of the sinusoidal sweep is chosen as $\zeta_S = 8$ kHz/s. The performance of the amplitude and phase controller is illustrated for a gyroscope with (A) an increased damping parameter $\hat{\alpha}_1 = 1.33 \alpha_1$, (B) the nominal damping parameter $\hat{\alpha}_1 = \alpha_1$ and (C) a decreased damping parameter $\hat{\alpha}_1 = 0.5 \alpha_1$.

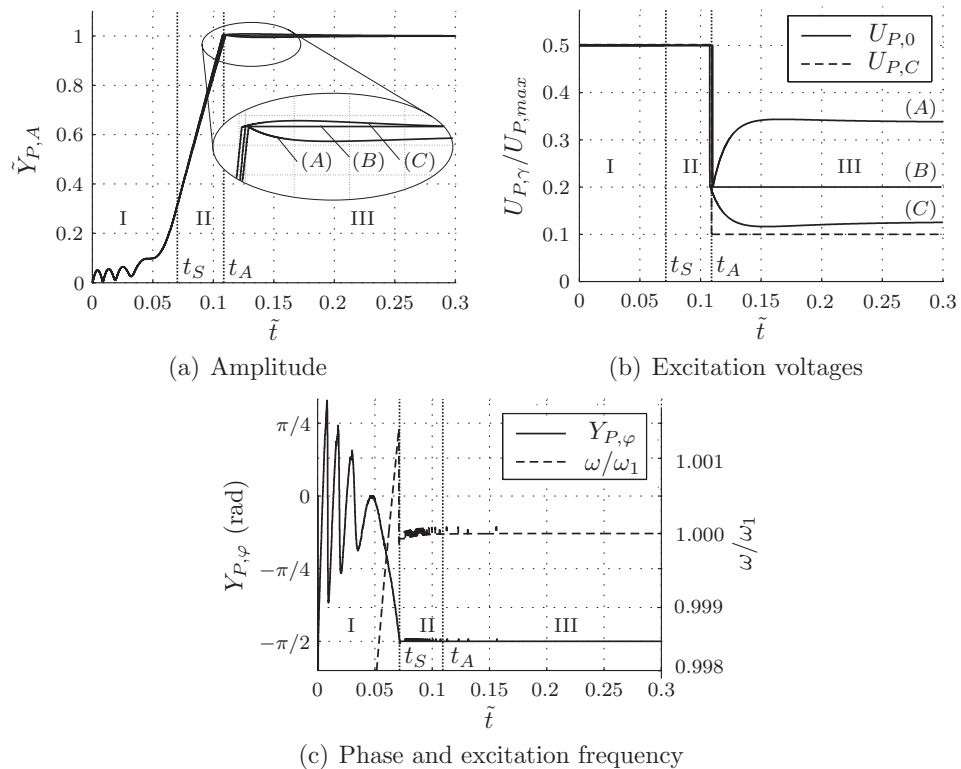


Figure 4: Start-up phase of the primary control in terms of (a) the normalized amplitude $\tilde{Y}_{P,A}$, (b) the primary excitation voltages $U_{P,\gamma}$, $\gamma \in \{0, C\}$ and (c) the phase $Y_{P,\varphi}$ of the primary output voltage and the excitation frequency ω .

The time axis with $\tilde{t} = t/t_N$ in Fig. 4 is normalized to the time t_N , which is a predefined value marking the end of the start-up phase. For $t \geq t_N$ the gyroscope is considered to operate in the normal mode providing a reliable measurement output with a predefined accuracy for the externally applied angular rate Ω .

3.2. Control of the secondary oscillation

Typically, two modes of operation can be distinguished for vibratory MEMS gyroscopes, namely the *split mode*, if there is a predefined nominal difference between the primary and secondary eigenfrequency, and the *matched mode*, if the secondary eigenfrequency is controlled to match the primary eigenfrequency, see, e.g., [15]. Within this subsection, the focus is

laid on the derivation of a quadrature controller and a combined quadrature and force feedback controller for a sensor designed to operate in the split mode with a constant input \tilde{U}_T and thus a constant frequency difference $|\omega_1 - \omega_2| > 0$, respectively.

3.2.1. Quadrature control

Starting point for the following considerations is the envelope model of the secondary mode (11). The corresponding transfer function matrix from the input $\mathbf{U} = [\tilde{U}_{S,C}, \tilde{U}_C]^T$ to the output $\mathbf{Y} = [Y_{S,S}, Y_{S,C}]^T$ is given by

$$\mathbf{G}(s) = \frac{-\beta_{12}c_2}{(s + \alpha_2)^2 + (\omega_1 - \omega_2)^2} \begin{bmatrix} -(s + \alpha_2)\Gamma_F & (\omega_1 - \omega_2)\Gamma_C \\ (\omega_1 - \omega_2)\Gamma_F & (s + \alpha_2)\Gamma_C \end{bmatrix} \quad (21)$$

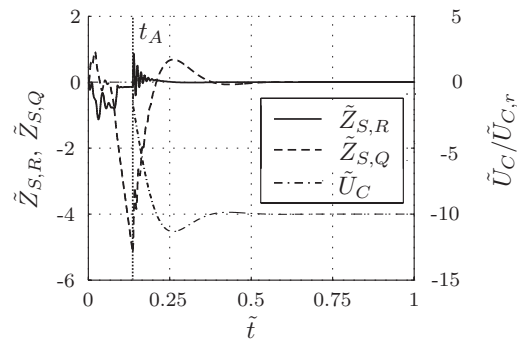
Considering the stationary decoupling by means of the transformation (12), the behavior of the MIMO system from the input \mathbf{U} to the transformed output $\mathbf{Z} = [Z_{S,R}, Z_{S,Q}]^T$ is described by the transfer function matrix

$$\mathbf{H}(s) = \mathbf{T}\mathbf{G}(s) = \begin{bmatrix} H_{11}(s) & H_{12}(s) \\ H_{21}(s) & H_{22}(s) \end{bmatrix} \quad (22)$$

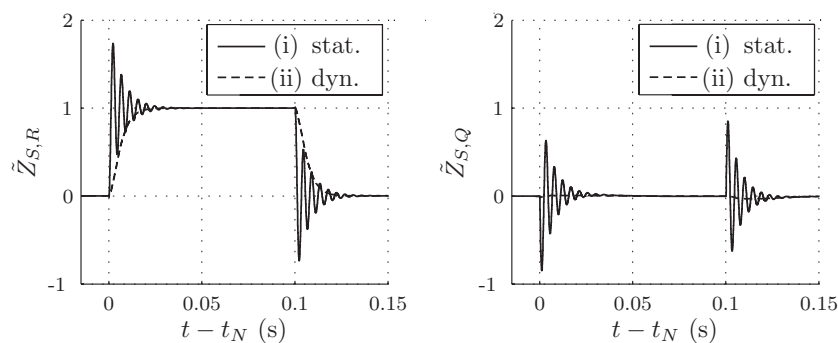
with $\lim_{s \rightarrow 0} H_{12}(s) = \lim_{s \rightarrow 0} H_{21}(s) = 0$.

In its simplest form, the control of the secondary mode merely covers the closed-loop control for the unbalance compensation, while the angular rate signal is obtained from the open-loop measurement output $Z_{S,R}$ of the gyroscope according to (13). Thus, the quadrature controller can be easily derived for the linear and time-invariant SISO system described by the transfer function $H_{22}(s)$. The demands on the closed-loop behavior are a predefined rise time and the exact suppression of a constant mechanical unbalance in the stationary case. The quadrature controller is activated at the time $t = t_A$ when it can be assumed that the phase controller is in steady state and thus the demodulation yields proper output signals $Z_{S,R}$ and $Z_{S,Q}$.

The dynamic behavior of the quadrature controller at the start-up phase is illustrated in Fig. 5(a). Again, the time axis is normalized in the form $\tilde{t} = t/t_N$. Moreover, the angular rate and quadrature signals are normalized in the form $\tilde{Z}_{S,\gamma} = Z_{S,\gamma}/Z_r$, $\gamma \in \{R, Q\}$ with the corresponding response Z_r to an angular rate of $\Omega = 100^\circ/\text{s}$. Likewise, the input \tilde{U}_C is normalized to the corresponding value $\tilde{U}_{C,r}$ required to compensate an unbalance of $\Gamma_M = 100^\circ/\text{s}$. The simulated gyroscope possesses an unbalance of $\Gamma_M = 1000^\circ/\text{s}$.



(a) Start-up phase



(b) Normal mode of operation

Figure 5: Dynamic behavior of the quadrature controller (a) in the start-up phase and (b) in the normal mode of operation in response to a step input of the external angular rate Ω in the case of (i) stationary and (ii) dynamic decoupling.

The dynamic response of the closed-loop system to an input step of the angular rate Ω in terms of the normalized quantities $\tilde{Z}_{S,R}$ and $\tilde{Z}_{S,Q}$ is illustrated in Fig. 5(b). It can be clearly seen that, although the angular rate signal $\tilde{Z}_{S,R}$ and the quadrature signal $\tilde{Z}_{S,Q}$ are stationarily decoupled, they show a strong coupling in the transient phase. Furthermore, due to the considered open-loop measurement of the angular rate the weakly damped system dynamics cannot be influenced in the output signal $\tilde{Z}_{S,R}$. In order to eliminate these unwanted system characteristics, in the next step a closed-loop force feedback controller comprising a dynamic decoupling of the output signals will be derived.

3.2.2. Combined quadrature and force feedback control

If the output transformation is performed by means of the transfer function matrix

$$\mathbf{T}(s) = S \frac{\alpha_2}{\beta_{12}c_2} \begin{bmatrix} -1 & \frac{\omega_1 - \omega_2}{s + \alpha_2} \\ \frac{\omega_1 - \omega_2}{s + \alpha_2} & 1 \end{bmatrix} \quad (23)$$

the MIMO system (11) can be dynamically decoupled such that the transfer behavior of the MIMO system (11) from the input \mathbf{U} to the transformed output \mathbf{Z} is given by the transfer function matrix

$$\mathbf{K}(s) = \mathbf{T}(s) \mathbf{G}(s) = \begin{bmatrix} K_1(s) & 0 \\ 0 & K_2(s) \end{bmatrix} \quad (24)$$

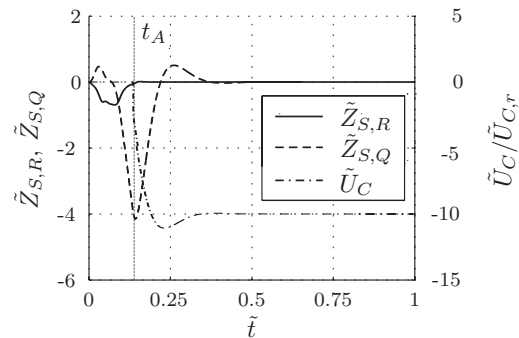
with the diagonal components

$$K_1(s) = -S \frac{\alpha_2 \Gamma_F}{s + \alpha_2} \quad \text{and} \quad K_2(s) = -S \frac{\alpha_2 \Gamma_C}{s + \alpha_2} .$$

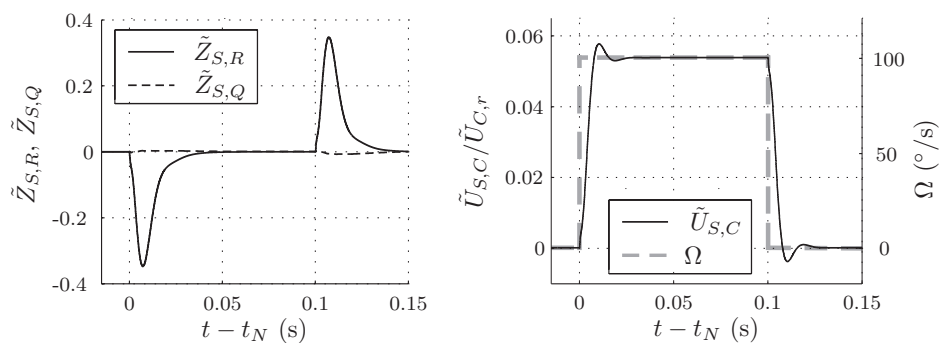
The constant factor $S \alpha_2 / (\beta_{12}c_2)$ in (23) is introduced in order to achieve the stationary solution $\lim_{s \rightarrow 0} K_{1(2)}(s) = -S \Gamma_{F(C)}$.

Now, the design of the quadrature controller from Sec. 3.2.1 can be performed on the basis of the linear time-invariant SISO system $K_2(s)$ instead of $H_{22}(s)$ which is dynamically decoupled from the system $K_1(s)$. The corresponding simulation results in the normal mode of operation can be found in Fig. 5(b). Additionally, a force feedback controller can be designed independently for the system $K_1(s)$ with the following demands on the closed-loop behavior. The system should exhibit a predefined rise time and the output signal $Z_{S,R}$ has to be stationarily controlled to zero for a constant external angular rate Ω . The closed-loop control is again activated at the time $t = t_A$ but in this concept, however, the actual measurement output (the angular rate signal) is taken directly from the force feedback control input $\tilde{U}_{S,C}$.

Figure 6(a) illustrates the dynamic behavior of the combined quadrature and force feedback controller in the start-up phase. In the normal mode of operation, the closed-loop system responds to an input step of the external angular rate Ω as depicted in Fig. 6(b), where an almost perfect decoupling between the angular rate signal $\tilde{Z}_{S,R}$ and the quadrature signal $\tilde{Z}_{S,Q}$ can be observed during the dynamic response. The corresponding force feedback input $\tilde{U}_{S,C}$ as illustrated in Fig. 6(b) directly serves as the measurement output of the gyroscope.



(a) Start-up phase



(b) Normal mode of operation

Figure 6: Dynamic behavior of the combined quadrature and force feedback controller (a) in the start-up phase and (b) in the normal mode of operation in response to a step input of the external angular rate Ω .

In contrast to the basic control concept the combined, dynamically decoupled concept of quadrature and force feedback control allows for actively tuning the closed-loop dynamics of the gyroscope. This advantage can be directly seen by comparing the response of the measurement output in Fig. 5(b), i.e. the angular rate signal, whose dynamic behavior is inherently given by the open-loop dynamics of the system (the natural damping and eigenfrequency of the secondary mode), with the response of the measurement output in Fig. 6(b), i.e. the force feedback input signal, which is tuned by the appropriate control design. The combined control concept including force feedback therefore is essential in particular if the natural damping of the secondary mode is small and the necessary bandwidth of the measurement output cannot be achieved in open-loop. However, the drawback of this method, besides

the slightly increasing electronic circuit complexity, is that since the necessary force feedback input $\tilde{U}_{S,C}$ is small compared to the compensation input \tilde{U}_C (a factor of approximately 15 for the gyroscope under consideration) the demands on the resolution of the corresponding DACs are increasing.

In reality, the model parameters $\hat{\alpha}_2$, $\hat{\omega}_2$, $\hat{\beta}_{12}$ and \hat{c}_2 differ from the nominal values α_2 , ω_2 , β_{12} and c_2 thus necessitating an appropriate calibration procedure. For the basic control concept discussed in Subsec. 3.2.1 this can simply be realized by adjusting the demodulation of the secondary mode signal, i.e. the output transformation (12), which directly yields the parameter $\hat{\phi}$. For the combined control concept the frequency difference $\hat{\omega}_1 - \hat{\omega}_2$ can be obtained in a similar manner by adjusting the demodulation of the secondary mode signal, i.e. the output transformation (23) in steady state, cf. $K_1(s)$ and $K_2(s)$ in (24) for $s \rightarrow 0$. Then, a stationary decoupling of the measurement output is achieved. In order to improve the closed-loop performance and to realize a dynamical decoupling as proposed in Subsec. 3.2.2 also the damping parameter $\hat{\alpha}_2$ has to be identified by means of standard procedures for second order linear systems.

4. Experimental validation

To verify the control concepts introduced in Sec. 3 the corresponding controllers were implemented on a development board consisting of a Field Programmable Gate Array (FPGA) and additional analog circuitry for the actuation and read-out of a prototype capacitive gyroscope with an unbalance of $\Gamma_M = 830^\circ/\text{s}$. Special emphasis was placed on solely utilizing such logic resources of the FPGA which are available in standard ASIC processes. This is of particular importance especially in view of the targeted mass production of the considered MEMS gyroscopes.

The zero crossing of the primary mode signal is detected by a discrete external comparator which together with a digital phase frequency detector provides the signal $\Delta Y_{P,\varphi}$. The primary and secondary mode signals are converted from the analog to the digital domain and the signal $\Delta Y_{P,A}$ is derived by calculating the magnitude of the primary mode signal, while $Z_{S,R}$ and $Z_{S,Q}$ are obtained by an appropriate demodulation of the secondary mode signal.

The measurement results of the start-up strategy for the primary oscillation illustrated in Fig. 7 are in good accordance with the numerical simulation

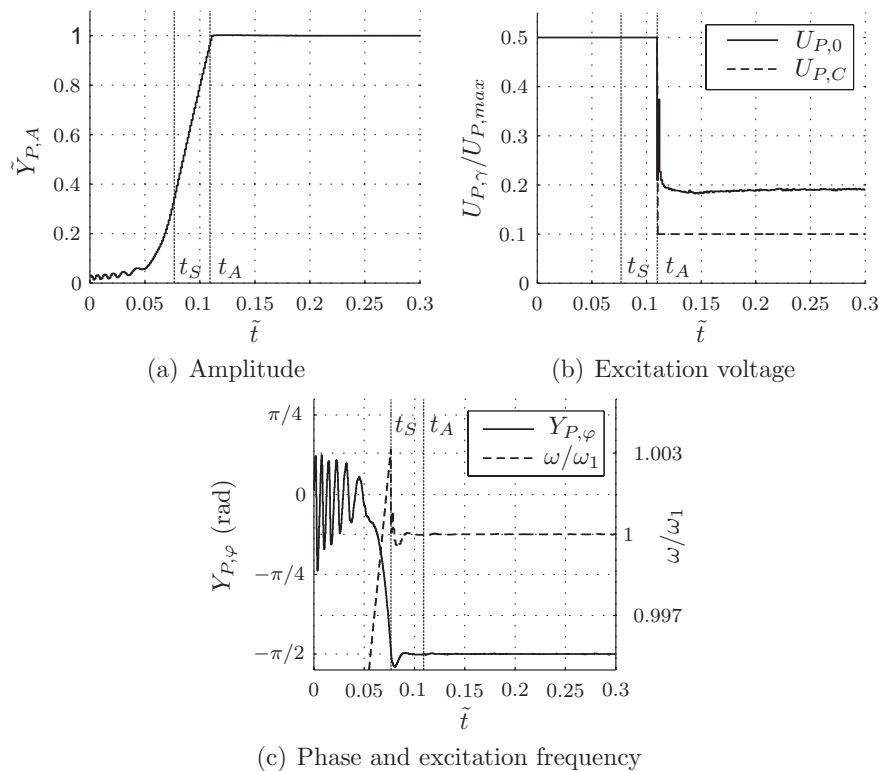
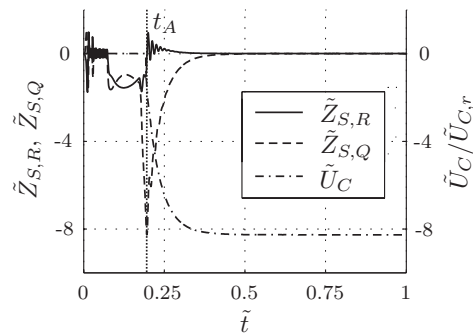


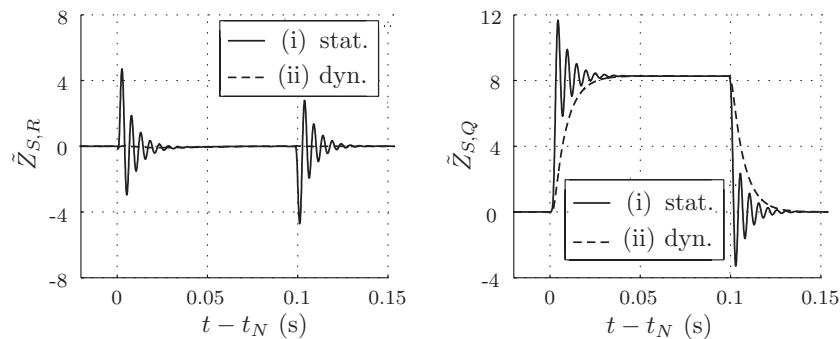
Figure 7: Measurement results of the start-up strategy for the primary mode in terms of (a) the normalized amplitude $\tilde{Y}_{P,A}$, (b) the voltages $U_{P,\gamma}$, $\gamma \in \{0, C\}$ and (c) the phase $Y_{P,\varphi}$ and the excitation frequency ω .

results presented in Sec. 3.1, cf. Fig. 4, and therefore validate the proposed mathematical model as well as the developed control concepts.

Also the measurement results of the secondary control in terms of the quadrature controller during the start-up phase, illustrated in Fig. 8(a), as well as the results obtained from the combined quadrature and force feedback controller, illustrated in Fig. 9(a), show the same excellent behavior as the numerical simulation results presented in Sec. 3.2, cf. Figs. 5(a) and 6(a). Since in reality the development board cannot be exposed to a step-like angular rate, the stationary and dynamic output transformation was verified by measuring the quadrature and angular rate signal in response to a step of the compensation input voltage \tilde{U}_C . The feasibility of this approach can directly be obtained from (11) by substituting Ω for $\Gamma_C \tilde{U}_C$. The measurement



(a) Start-up phase

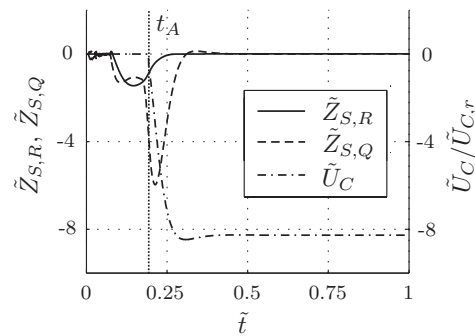


(b) Normal mode of operation

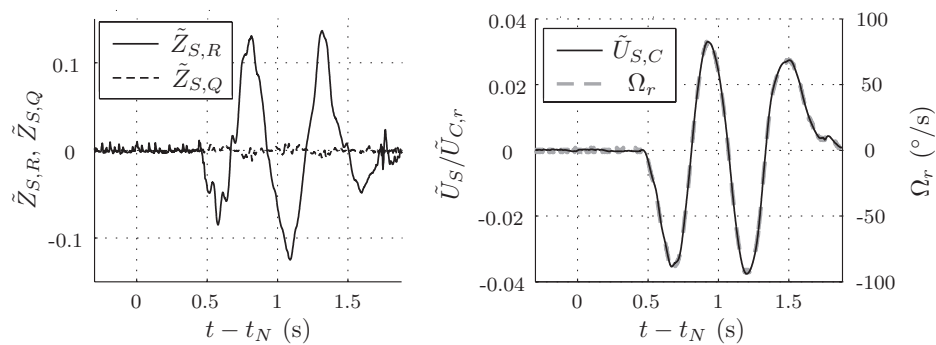
Figure 8: Measurement results of the dynamic behavior of the quadrature controller (a) in the start-up phase and (b) in the normal mode of operation in response to a step of the compensation input \tilde{U}_C in the case of (i) stationary and (ii) dynamic decoupling.

results, depicted in Fig. 8(b), show the expected transient coupling between the normalized rate and quadrature signals for the stationary output transformation and a nearly perfect decoupling of the signals for the dynamic output transformation. However, in comparison with the simulation results obtained in Sec. 3.2 the quadrature signal in Fig. 8(b) is equivalent to the angular rate signal in Fig. 5(b) and vice versa due to the different excitation in terms of the compensation input \tilde{U}_C instead of an external angular rate Ω .

The actual closed-loop response of the combined concept with quadrature and force feedback control due to an external angular rate Ω is illustrated in Fig. 9(b). Here, the angular rate is applied by manually turning the



(a) Start-up phase



(b) Normal mode of operation

Figure 9: Measurement results of the dynamic behavior of the combined quadrature and force feedback controller (a) in the start-up phase and (b) in the normal mode of operation in response to a manually applied external angular rate Ω_r .

development board. The applied angular rate Ω is measured with a calibrated reference sensor yielding the measurement output Ω_r . As can be observed, the normalized compensation input $\tilde{U}_{S,C}$ is perfectly tracking the reference Ω_r , whereas the angular rate and quadrature signals $\tilde{Z}_{S,R}$ and $\tilde{Z}_{S,Q}$, remain decoupled during the complete transition.

5. Summary

The paper presents a systematic design of open- and closed-loop controllers for vibratory MEMS gyroscopes based on so-called envelope models. As an illustrative example an optimized start-up strategy for the primary mode of a capacitive gyroscope is derived highlighting the advantages of the

presented methodology. Furthermore, the approach is also utilized for the systematic design of a basic quadrature controller for the secondary mode in order to compensate for the inherent unbalance effects caused by the non ideal fabrication process. In order to eliminate the typically weakly damped open-loop dynamics of the gyroscope and the transient coupling between the quadrature and the angular rate signal a more sophisticated combined concept of closed-loop quadrature and force feedback control was introduced. Simulation and measurement results for a prototype gyroscope validate the mathematical models and prove the feasibility of the proposed control concepts.

Acknowledgements

This work was funded by the German BMBF as part of the EURIPIDES project RESTLES (project no. V3EUR015).

Nomenclature

Throughout the paper the indices $j = 1, \dots, n$ and $i = 1, \dots, m$ are used to identify the respective vibratory mode and the movable electrodes. In this contribution the number of vibratory modes is chosen as $n = 2$. The index $\alpha \in \{P, S\}$ refers to the primary and secondary mode while the index $\beta \in \{S, C\}$ denotes the sine and cosine Fourier coefficient of the respective harmonic signal.

The entire list of symbols can be found in the following Tables 1 to 4. Quantities denoted with a tilde symbol are normalized with respect to a reference value and quantities denoted with a hat symbol are real parameter values differing from the nominal values. The system linearized about a desired operating point (equilibrium) referred to with a * symbol is described in terms of small deviations Δ .

References

- [1] Ezekwe CD, Boser BE. A mode-matching $\Delta\Sigma$ closed-loop vibratory readout interface with a $0.004^\circ/\text{s}/\text{Hz}$ noise floor over a 50 Hz band. In: Proc. of the 2008 IEEE Int. Solid-State Circuits Conference. San Francisco, USA; 2008, p. 580–1.

t	Time
q_j	Vibratory modes
Ω, ξ	Angular rate and side wall angle
m_j, d_j, k_j	Inertia, damping and stiffness coefficients
c_{12}, k_{12}, f_j	Coriolis, unbalance and electromechanical coupling coefficient
$b_j, k_{12,C}, k_{2,T}$	Input coefficients
c_j	Output coefficients
$u_P, u_{S,i}$	Primary and secondary input voltages
x_i, z_i	Translational degrees of freedom
r_i, s_i	Positive constants
g_i, t_i, A_i, l_i	Gap, width, overlap area, overlap length
ε_0, C_i, W_i	Dielectric coefficient, capacitance and potential energy
$\tilde{u}_\alpha, \tilde{u}_C, \tilde{u}_T$	Transformed input for harmonic excitation, unbalance compensation and frequency tuning
y_α	Primary and secondary output voltage

Table 1: List of symbols concerning the general dynamical model.

- [2] Kuisma H, Ryhänen T, Lahdenperä J, Punkka E, Routsalainen S, Silanpää T, et al. A bulk micromachined angular rate sensor. In: Proc. of the 9th Int. Conf. on Solid-State Sensors, Actuators and Microsystems, Transducers '97. Chicago, USA; 1997, p. 875–8.
- [3] Loveday PW, Rogers CA. The influence of control system design on the performance of vibratory gyroscopes. *Journal of Sound and Vibration* 2002;255:417–32.
- [4] Maenaka K, Fujita T, Konishi Y, Maeda M. Analysis of a highly sensitive silicon gyroscope with cantilever beam as vibrating mass. *Sensors and Actuators A: Physical* 1996;54:568–73.
- [5] Geiger W, Butt WU, Gaißer A, Frech J, Braxmaier M, Link T, et al. Decoupled microgyros and the design principle DAVED. *Sensors and Actuators A: Physical* 2002;95:239–49.
- [6] Egretzberger M, Kugi A. A dynamical envelope model for vibratory gyroscopes. *Microsystem Technologies* 2010;16:777–86.
- [7] Bhave SA, Seeger JI, Jiang X, Boser BE, Howe RT, Yasaitis J. An integrated vertical-drive, in-plane-sense microgyroscope. In: Proc. of

ω	Excitation frequency
$U_{P,0}, U_{P,C}$	Fourier coefficients of the primary excitation voltage
$Q_{j,\beta}$	Fourier coefficients of the vibratory modes
$\tilde{U}_{\alpha,\beta}$	Fourier coefficients of the harmonic inputs
\tilde{U}_C, \tilde{U}_T	Fourier coefficients of the slowly varying inputs
$Y_{\alpha,1}$	Fourier coefficients of the output voltages
$\alpha_j, \beta_j, \omega_j$	Damping and input coefficients, eigenfrequencies
$Y_{P,A}, Y_{P,\varphi}$	Amplitude and phase of the primary output voltage
$Y_{P,des}$	Desired amplitude of the primary output voltage
$\beta_{12}, \Gamma_F, \Gamma_M, \Gamma_C$	Input coefficients
$Z_{S,R}, Z_{S,Q}$	Angular rate and quadrature output signal
\mathbf{Y}, \mathbf{Z}	Output vectors
\mathbf{T}	Output transformation matrix
S	Sensitivity

Table 2: List of symbols concerning the envelope model.

ω_0, ζ_S	Ramp start frequency and slope
$\omega_S, \bar{\omega}_1$	Frequency at time t_S , identified frequency
$U_{P,max}, U_{P,ctrl}$	Maximum primary excitation voltage, fixed excitation constant
Q_1	Quality factor of the primary mode
t_0, t_S, t_A, t_N	Time events
$G_{P,\varphi}, G_{P,A}$	Transfer functions for the primary control
s	Laplace variable

Table 3: List of symbols concerning the primary control.

the 12th Int. Conf. on Solid-State Sensors, Actuators and Microsystems, Transducers '03. Boston, USA; 2003, p. 171–4.

- [8] Alper SE, Akin T. A symmetric surface micromachined gyroscope with decoupled oscillation modes. *Sensors and Actuators A: Physical* 2002;97-98:347–58.
- [9] Braxmaier M, Gaißer A, Link T, Schumacher A, Simon I, Frech J, et al. Cross-coupling of the oscillation modes of vibratory gyroscopes. In: *Proc. of the 12th Int. Conf. on Solid-State Sensors, Actuators and Microsystems, Transducers '03. Boston, USA; 2003, p. 167–70.*
- [10] Seshia AA, Howe RT, Montaguët S. An integrated microelectromechan-

G	System transfer function matrix
U	Input vector
H, K	Stationary and dynamically decoupled transfer function matrices
$Z_r, \tilde{U}_{C,r}, \tilde{\Omega}_r$	Reference quantities

Table 4: List of symbols concerning the secondary control.

ical resonant output gyroscope. In: Proc. of the 15th IEEE Int. Conf. on Micro Electro Mechanical Systems. Las Vegas, USA; 2002, p. 722–6.

- [11] Günthner S. Entwurf und Charakterisierung von mikromechanischen Drehratensensoren in Silizium. Aachen: Shaker; 2006.
- [12] Merz P, Pilz W, Senger F, Reimer K, Grouchko M, Pandhumsoporn T, et al. Impact of Si DRIE on vibratory MEMS gyroscope performance. In: Proc. of the 14th Int. Conf. on Solid-State Sensors, Actuators and Microsystems, Transducers & Eurosensors '07. Lyon, France; 2007, p. 1187–90.
- [13] Seeger JI, Boser BE. Charge control of parallel-plate, electrostatic actuators and the tip-in instability. IEEE Journal of Microelectromechanical Systems 2003;12:656–71.
- [14] Mair F, Egretzberger M, Kugi A. A tool for the automatic modeling of capacitive MEMS gyroscopes. In: Proceedings of the 6th Vienna International Conference on Mathematical Modelling. Vienna, Austria; 2009, p. 2228–35.
- [15] Ayazi F, Zaman MF, Sharma A. Vibrating gyroscopes. In: Gianchandani YB, Tabata O, Zappe H, editors. Comprehensive Microsystems. Amsterdam: Elsevier; 2008, p. 181–208.
- [16] Egretzberger M. Mathematical Modeling and Control of Micro Electromechanical Gyroscopes. Aachen: Shaker; 2010.